ASTROBIOLOGY
Volume 13, Number 10, 2013

DOI: 10.1089/ast.2013.1034

Raman Hyperspectral Imaging of Microfossils: Potential Pitfalls

Craig P. Marshall and Alison Olcott Marshall

Abstract

Initially, Raman spectroscopy was a specialized technique used by vibrational spectroscopists; however, due to rapid advancements in instrumentation and imaging techniques over the last few decades, Raman spectrometers are widely available at many institutions, allowing Raman spectroscopy to become a widespread analytical tool in mineralogy and other geological sciences. Hyperspectral imaging, in particular, has become popular due to the fact that Raman spectroscopy can quickly delineate crystallographic and compositional differences in 2-D and 3-D at the micron scale. Although this rapid growth of applications to the Earth sciences has provided great insight across the geological sciences, the ease of application as the instruments become increasingly automated combined with nonspecialists using this techique has resulted in the propagation of errors and misunderstandings throughout the field. For example, the literature now includes misassigned vibration modes, inappropriate spectral processing techniques, confocal depth of laser penetration incorrectly estimated into opaque crystalline solids, and a misconstrued understanding of the anisotropic nature of sp^2 carbons. Key Words: Raman spectroscopy—Raman imaging—Confocal Raman spectroscopy—Disordered sp^2 carbons—Hematite—Microfossils. Astrobiology 13, 920–931.

1. Introduction

Although Raman spectroscopy has only been applied in paleobiology for the last 34 years (*e.g.,* Pflug and Jaeschke-Boyer, 1979), the technique is decades older. In 1928, Sir C.V. Raman first reported the Raman effect, which is the inelastic scattering of light (*e.g.,* Raman, 1928; Raman and Krishnan, 1928a, 1928b). In the first decade after its discovery, nearly 2000 papers on the Raman effect were published, and the Raman spectra of more than 2500 compounds were reported. The advent of the laser (Light Amplification by Stimulated Emission of Radiation) in the early 1960s revolutionized the practice and application of Raman spectroscopy to many disciples outside vibrational spectroscopy. By the end of 1978, the 50th anniversary of Raman's discovery, 24,000 papers dealing with various kinds of Raman effect had been published. Raman spectroscopy is becoming increasingly popular in geoscience applications, as astrobiologists, geologists, paleontologists, and planetary and space scientists discover the wealth of nondestructive mineral and organic molecule/macromolecule data that Raman spectroscopy can afford (*e.g.,* Jehlička and Bény, 1992, 1999; Wopenka and Pasteris, 1993; Beyssac *et al.,* 2002; Wang *et al.,* 2004, 2006; Marshall *et al.,* 2010, 2011; Olcott Marshall *et al.,* 2012a, 2012b; Edwards *et al.,* 2013).

Fossilized microbes are a frequently named target of life-detection missions on Mars (*e.g.,* Des Marais *et al.,* 2008). Researchers are using Raman spectroscopy to access the composition of putative microfossils as an additional line of evidence for microbial life in the rock record (*e.g.,* Pflug and Jaeschke-Boyer, 1979; Pflug, 1984; Ueno *et al.,* 2001a, 2001b; Schopf *et al.,* 2002, 2010; Schopf and Kudryavtsev, 2005, 2009; Edwards *et al.,* 2007; Schiffbauer *et al.,* 2007, 2012; Kazmierczak and Kremer, 2009; Marshall and Olcott Marshall, 2011; Marshall *et al.,* 2011; Kremer *et al.,* 2012a; Meyer *et al.,* 2012). The ESA/NASA ExoMars planetary mission proposed for launch in 2018 will contain a miniaturized Raman spectrometer (RLS) as part of the Pasteur payload (Vago *et al.,* 2006).

Raman spectroscopy is rapidly becoming a technique used by nonspecialists, which has to some extent led to recent paleobiological and astrobiological literature affected by the publication of incorrectly assigned vibration modes, inappropriate spectral processing techniques, overestimated confocal depth of laser penetration into opaque crystalline solids, and a misconstrued understanding of the anisotropic nature of sp^2 carbons. The principal aim of this paper is to consider and discuss these problematic issues and encourage best spectroscopic practice as a standard way forward for future applications of Raman hyperspectral imaging in paleobiology and astrobiology research.

Department of Geology, University of Kansas, Lawrence, Kansas.

2. Raman Spectroscopy and Hyperspectral Imaging

Given the misconceptions pertaining to vibration mode assignments, depth of laser penetration during confocal analyses, and hyperspectral imaging, it is relevant here to concisely review the phenomena of Raman scattering, confocal Raman spectroscopy, and hyperspectral imaging. Raman spectroscopy is a nondestructive, non-invasive analytical technique that affords information about the molecular composition and structure of a sample. The sample is irradiated with an incident monochromatic light from a laser, that is, UV, visible (vis), or near-IR (NIR) excitation, and photons are either inelastically or elastically scattered. The inelastically scattered light, known as Raman scatter, has lost (Stokes) or gained (anti-Stokes) energy/frequency during interaction with molecules or crystals, and the emitted photon contains information about the molecular structure and symmetry of the sample. The change in frequencies (Raman shift Δ cm^{-1}) depends on the masses of the atoms involved in the vibration (*i.e.*, atomic identity, *e.g.*, C-C vs. Fe-O), on the bond strengths (force constants), and on the bond lengths and angles (geometry)—in other words, on all the parameters that constitute the structure of a molecule or crystal. Hence, Raman spectroscopy can be used to identify minerals and elucidate their degree of order (*i.e.*, short-range versus long-range atomic arrangements).

Confocal Raman spectroscopy involves using a confocal pinhole with associated lens or alternatively closing down the spectrograph entrance slit and reducing the height of the captured image on the CCD camera. This permits optical sectioning by acquiring spectra, as the laser focus is moved incrementally deeper into a NIR, vis, or UV transparent sample, which is termed *depth profiling*. The depth of laser penetration into a material depends upon the (i) refractive index (RI) of the material, (ii) wavelength of the laser, and (iii) the numerical aperture (NA) of the objective. Everall (2000) examined a variety of materials of differing RI and clearly demonstrated that the depth of penetration is primarily associated with the RI of the material.

With the advent of the Raman microprobe and mapping/imaging techniques pioneered by Rosasco *et al.* (1975) and Delhaye and Dhamelincourt (1975), Raman microspectroscopy and hyperspectral imaging have become established and routinely used in the geosciences.

Raman mapping and imaging are techniques that can be used to investigate the chemical (*e.g.*, molecular species, and chemical bonds) and mechanical (*e.g.*, stress of a phase) properties of a sample with respect to their 2-D and 3-D spatial distribution on the micrometer scale. This is achieved by producing false-color images, which allow visualization of the type and spatial distribution of chemical and mechanical features within a sample. Spectra are collected sequentially point by point or raster-scanned in two spatial dimensions over a defined region typically over areas of tens to hundreds of micrometers, with a user-defined step size in both x and y directions. Therefore, this data set could consist of tens of thousands of Raman spectra. A 4-D data hypercube is produced that includes a spectrum, a plot of Raman shift (Δ cm^{-1}) against intensity (arbitrary units), and the spatial coordinates from where the spectrum was collected (x, y). The collected 2-D hyperspectral images acquired from optical sectioning can be stitched together by imaging software to generate 3-D images.

3. Materials and Methods

3.1. Raman microspectroscopic analyses

Standard point Raman spectra, 2-D, and 3-D images were collected on thin sections with a Renishaw inVia Reflex Raman Microprobe (Renishaw plc, Wotton-under-Edge, UK), equipped with a Peltier cooled CCD camera (1024×256 pixels). The spectrometer is fitted with holographic notch filters and five gratings [3600 mm/line (UV), 2400 mm/line (vis), 1800 mm/line (vis), 1200 mm/line (NIR), and 830 mm/line (NIR)]. The Raman light was dispersed by a diffraction grating with 2400 mm/line, and the signal was analyzed with a Peltier cooled CCD camera at room temperature (1024×256 pixels). The attached microscope is a Leica DM LM and is equipped with four objectives (×100/0.9 NA, ×50/0.75 NA, ×20/0.40 NA, ×5/0.12 NA) and a trinocular viewer that accommodates a video camera that allows direct viewing of the sample. Sample excitation was achieved with an argon ion laser (Modu-Laser, Utah, USA) emitting at a wavelength of 514.5 nm. The laser power impinging on the thin sections was between 1 and 5 mW in order to minimize laser-induced heating of the samples such as disordered sp^2 hybridized carbonaceous materials and hematite (*cf.*, Marshall *et al.*, 2010). Calibration of the Raman shift is achieved by recording the Raman spectrum of the silicon TO (traversal optical) phonon F_{1g} mode for one accumulation and 10 s. If necessary, an offset correction is performed to ensure that the position of the F_{1g} band is at 520.50 ± 0.10 Δ cm^{-1}. It is standard practice to calibrate the confocal system by performing a depth profile on a silicon wafer (the F_{1g} band at 520.50 ± 0.10 Δ cm^{-1}). The spectrometer is controlled by using Renishaw WiRE version 3.3 software. Raman images were made by collecting in StreamLine mode with an accumulation time of 0.1–2.0 s and collected over the spectral region 500–1800 Δ cm^{-1} and optically sectioning every 1.0 μm down into the thin section from 1.0 μm to a depth of 25.0 μm.

3.2. Spectroscopic pre-processing of data and rationale

It is standard practice by spectroscopists that spectra have to be pre-processed before producing 2-D or 3-D images. Preprocessing should take into account baseline effects, and spectra should be properly normalized. Common baseline effects associated with Raman spectra collected from geological samples are a sloping enhanced background, which is caused by fluorescence. Wopenka (2012) clearly showed that geological carbonaceous particles have a varying response in laser-induced autofluorescence throughout individual particles. Therefore, polynomials of various orders are used to eliminate broad autofluorescence baselines.

Here, pre-processing and data analysis were performed with Renishaw WiRE 3.3 software. Pre-processing of data consisted of (i) cosmic ray removal, (ii) baseline correction, and (iii) normalization. First, cosmic rays were removed from the spectral data by using a nearest neighbor cosmic removal method. Second, the spectra were baseline corrected with a 5th-order polynomial to remove any sloping-enhanced background due to autofluorescence. Third, all the data were band-intensity normalized to 1.0 with respect to the highest intensity band in the spectrum. This third step is an

important procedure of pre-processing to generate 2-D and 3-D images, as this procedure eliminates intensity deviations between many measured data points that can result in false highs and lows for a chosen vibration mode particularly in samples displaying spatial variation in autofluorescence.

3.3. Raman image generation

To generate Raman images, the intensity of a particular band at each spatial location is plotted to produce an image. This method is widely used in the spectroscopy community (*e.g.*, McCreery, 2000) and provides information about the spatial location of every molecule or bond within the sample that contributes intensity to the vibration mode frequency chosen. However, care must be taken in this approach, as this can potentially lead to incorrect band assignment (see below for further discussion). False-color images shown in Fig. 5 were generated by using the intensity of the band maxima of the hematite 2LO ($2E_u$) mode at 1320 Δ cm^{-1}, D mode (A_{1g}) at 1350 Δ cm^{-1}, and G mode (E_{2g2}) at 1600 Δ cm^{-1} to reveal the relative composition locations.

4. Results

Here, we present Raman spectra, confocal depth profiles, and hyperspectral images obtained from embedded microstructures and mineralogical features from 300 μm thick thin sections made from the *ca.* 3.5 Ga Apex chert hydrothermal vein (refer to Marshall *et al.*, 2011; Olcott Marshall *et al.*, 2012a for locality and thin section details) and research-grade hematite 49-5908 purchased from Wards Natural Science.

4.1. Confocal Raman microspectroscopy: penetration depth in thin sections of black chert

The stacked spectra in the depth profile series (Fig. 1a) clearly show a significant decrease in the band at 464 Δ cm^{-1} assigned to the ν_sSi-O-Si symmetric stretching mode (A_1 symmetry mode) of α quartz, and the G band at 1600 Δ cm^{-1} [assigned to a doubly degenerate TO and LO (longitudinal optical) phonon mode corresponding to the E_{2g2} mode of graphite with D^4_{6h}point group symmetry] and D band at 1350 Δ cm^{-1} (a phonon mode that becomes Raman-allowed when defects are introduced to the lattice or decreasing dimension of crystallites occurs with A_{1g} symmetry) at a depth of 15 μm, and the data becomes unreliable at a depth of 20 μm due to an unacceptable signal-to-noise ratio. Alternatively, the spectra acquired from the depth profile series can be plotted as a false-color image (Fig. 1b). This is perhaps most useful when considering how deep within a sample a false-color hyperspectral image should be constructed when using the intensity of a particular band of interest. Figure 1b shows that using the intensity of the G band, D band, and A_1 quartz band would be limited to a depth of 6, 8, and 14 μm, respectively.

4.2. Polarization effects on spectra acquired from sp^2 carbonaceous materials

Figure 2 shows a stack plot of Raman spectra acquired from pure hexagonal graphite with the incident laser beam either perpendicular or parallel to the *c* axis. The spectrum colored black in the plot was acquired with the incident laser beam parallel (||) to the *c* axis, and the spectrum colored gray was acquired with the incident laser beam perpendicular ($\perp$) to the *c* axis. The spectrum acquired || to the *c* axis shows greater D band intensity ($I_D/I_G = 0.40$) relative to the normalized G band, while the spectrum acquired $\perp$ to the *c* axis shows lower D band intensity ($I_D/I_G = 0.15$) relative to the normalized G band (Fig. 2). Figure 3 shows a plot of Raman spectra acquired from disordered sp^2 carbon from the Apex chert with the incident laser beam either perpendicular or parallel to the *c* axis. The spectrum colored black in the plot was acquired with the incident laser beam parallel (||) to the *c* axis, and the spectrum colored gray was acquired with the incident laser beam perpendicular ($\perp$) to the *c* axis (Fig. 3). These spectra clearly reveal that there is no change in the intensity of the D band relative to the G band as the orientation changes (*i.e.*, || $I_D/I_G = 1.20$ and $\perp I_D/I_G = 1.20$) (Fig. 3).

4.3. Raman spectra of sp^2 carbonaceous material and hematite

Figure 4 shows a stack plot of spectra collected from disordered sp^2 carbonaceous material and hematite in the carbon first-order frequency region (1000–1800 Δ cm^{-1}). The spectrum colored black in the plot was acquired on disordered sp^2 carbonaceous material, and the spectrum colored gray in the plot was acquired on hematite. The spectrum acquired from the sp^2 disordered carbonaceous material shows two broad intense bands at 1600 and 1350 Δ cm^{-1} assigned to the G band (a doubly degenerate TO and LO phonon mode corresponding to the E_{2g2} mode of graphite with D^4_{6h}point group symmetry) and the D band (a phonon mode that becomes Raman allowed when defects are introduced to the lattice or decreasing dimension of crystallites occurs with A_{1g} symmetry), respectively. The spectrum acquired from hematite shows one broad band at 1320 Δ cm^{-1}, which is assigned to a second-order 2LO mode with $2E_u$ symmetry due to defects in the hematite lattice.

4.4. Raman spectra of a mixture of sp^2 carbonaceous material and hematite

The Raman spectrum shown in Fig. 5 was acquired on a mixture of hematite and graphite. This spectrum contains a broad band between 1180 and 1450 Δ cm^{-1} centered at 1300 Δ cm^{-1} with a shoulder at 1345 Δ cm^{-1}, and a narrow band centered at 1575 Δ cm^{-1}. The line-shape, shoulder, and band positions are indicative of a Raman spectrum collected from a mixed hematite and sp^2 carbonaceous material phase. This spectrum contains overlapping bands, which can be resolved by deconvolution into four Gaussian-Lorentzian components at 1575, 1345, 1300, and 1095 Δ cm^{-1} (Fig. 5) (refer to Marshall *et al.*, 2010, for further discussion on deconvolution in the carbon first-order region). The bands at 1575, 1345, and 1300 Δ cm^{-1} are assigned to the G band of sp^2 carbonaceous material, D band of sp^2 carbonaceous material, and the 2LO mode of disordered hematite, respectively.

4.5. Hyperspectral images

Figure 6 shows hyperspectral images generated from research-grade hematite 49-5908 when using the following band position intensities: 1320 Δ cm^{-1} for the hematite 2LO mode at 1320, 1350 Δ cm^{-1} (D band) to establish the influence of the 2LO hematite mode on the hyperspectral image, and

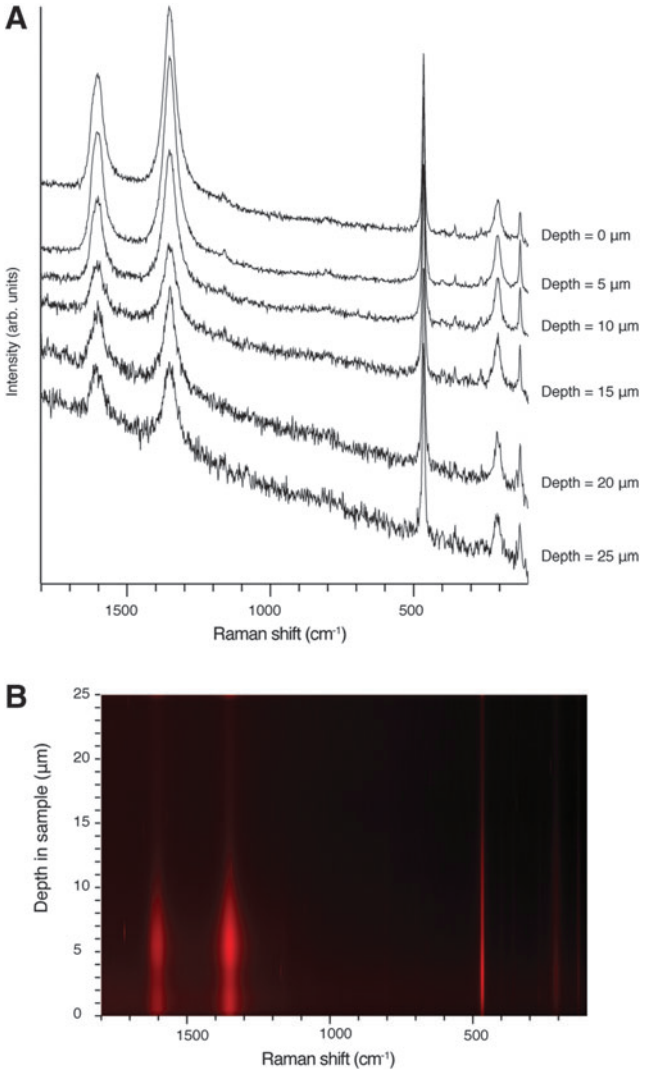

FIG. 1. (**A**) Stacked spectra in depth profile series showing a significant decrease in the band at 464 Δ cm^{-1} assigned to the ν_sSi-O-Si symmetric stretching mode (A_1 symmetry mode) of α quartz, and the G band at 1600 Δ cm^{-1} (assigned to a doubly degenerate TO and LO phonon mode corresponding to the E_{2g2} mode of graphite with D^4_{6h} point group symmetry) and D band at 1350 Δ cm^{-1} (a phonon mode that becomes Raman-allowed when defects are introduced to the lattice or decreasing dimension of crystallites occurs with A_{1g} symmetry) at a depth of 15 μm, and the data becoming unreliable at a depth of 20 μm. (**B**) Hyperspectral image generated from the intensity of the G band, D band, and A_1 band with increasing depth into thin section.

1600 Δ cm^{-1} (G band) as a test of a marker band for carbonaceous material. In addition, representative raw spectra are shown from various regions of the hyperspectral image. The raw representative spectra show one broad band at 1320 Δ cm^{-1}, which is assigned to a second-order 2LO mode with $2E_u$ symmetry due to defects in the hematite lattice.

5. Discussion

The results obtained from the thin sections and research-grade hematite with reference to the potential of incorrectly assigned vibration modes, inappropriate spectral processing techniques, overestimated confocal depth of laser penetration into opaque crystalline solids, and a misconstrued understanding of the anisotropic nature of sp^2 carbons within the paleobiology and astrobiology literature are discussed here.

5.1. Depth of laser penetration in thin sections of black cherts

Raman microspectroscopy is a surface characterization technique with limited depth penetration into solid, optically opaque crystalline materials, such as thin sections made from black cherts. However, with the advent of confocal Raman microspectroscopy it is now possible to obtain the composition of the underlying subsurface features in opaque crystalline materials. In standard Raman point spectral acquisition, that is, non-confocal mode, the depth of laser penetration into opaque siliceous materials is in the order of 1 μm (see Marshall *et al.*, 2011, for discussion). In stark contrast, carbonaceous materials are black, opaque crystalline materials, and as such have a high extinction coefficient for visible light. When using a laser with an excitation wavelength of 514.5 nm in the visible range, the depth of penetration of the laser is low, approximately <200 nm into a carbonaceous material particle (Lespade *et al.*, 1984). Therefore, to optically section deeper into translucent to opaque crystalline solid to interrogate features of interest, confocal Raman analysis must be performed.

Studies by Schopf and Kudryavtsev (2005, 2009, 2012) of Precambrian black cherts containing embedded microstructures and microfossils of various mineral compositions report that they are able to penetrate to depths of 150 μm in a 300 μm thick thin section. This 150 μm depth of penetration is in disagreement with analyses by Kremer *et al.* (2012a) and our results presented here (Fig. 1). We clearly demonstrate that a depth of greater than 15 μm into thin sections of black cherts does not yield a sufficient enough signal even though we have employed standard Raman point spectral acquisition parameters of 10 s collections with 3 accumulations, compared to typical hyperspectral image collection parameters of only 1 accumulation time of 0.1–2.0 s. Clearly, using typical hyperspectral imaging conditions, data generated at depths greater than 15 μm would be unusable. Likewise, the work of Kremer *et al.* (2012a) also discusses the limitation of performing 3-D images at depths greater than 15–20 μm in thin sections of black cherts. Our results clearly show that the estimate of penetration depth of 150 μm into thin sections of black chert by Schopf and Kudryavtsev (2005, 2009, 2012) is unlikely to be correct. Calculating the depth of confocal penetration is not a trivial exercise, largely due to the difficulty in modeling a confocal profile in optically opaque heterogeneous materials. Therefore, we suggest caution upon reporting such depths and recommend that confocal depth profiles should be collected and presented like those shown in Fig. 1.

5.2. Polarization effects on spectra acquired from anisotropic minerals

If a crystalline solid has a lattice structure whose atoms are arranged or spaced differently when viewed in any or all of the three crystallographic axes (*a, b, c*), that crystal is termed

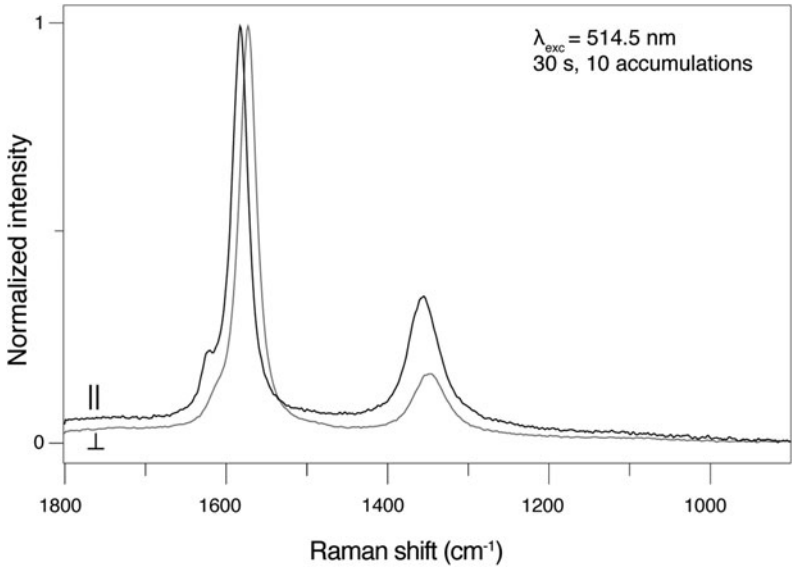

FIG. 2. Plot of Raman spectra acquired from pure hexagonal graphite with the incident laser beam either perpendicular or parallel to the *c* axis. The spectrum colored black was acquired with the incident laser beam parallel (||) to the *c* axis, and the spectrum colored gray was collected with the incident laser beam perpendicular (⊥) to the *c* axis.

anisotropic. The physical and mechanical properties of anisotropic crystalline materials will differ with respect to different crystallographic orientations. The Raman intensity of Raman-scattered radiation from anisotropic minerals strongly depends on the orientation of the crystal and the polarization of incident and scattered light (*e.g.,* Turrell, 1972). Raman scattering from an anisotropic mineral is associated with an induced change in polarizability in which amplitude depends on (i) the orientation of a crystal, (ii) scattering geometry, and (iii) polarization of the incident and scattered light (*e.g.,* Turrell, 1972). Raman scattering of plane-polarized light can result in scattered radiation that is either parallel (||) or perpendicular (⊥) to the *c* axis of anisotropic crystalline solids, which can result in an enhancement of Raman bands depending on *c*-axis parallel or *c*-axis perpendicular analysis. Polarized Raman spectra can be achieved by (1) introducing a ½ waveplate between the sample and monochromator or (2) rotating the sample on the stage between analyses, changing its orientation and subsequently the intensity of the Raman bands measured each time. Polarized Raman spectroscopy can give an insight into crystal orientation and vibration symmetry, by investigation of the depolarization ratio ($\rho = I_{\perp}/I_{\parallel}$ or $I_{depolarized}/I_{polarized}$) of polarized Raman spectra.

Therefore, it is appropriate to review the crystallography of graphite and graphitic-like carbons here to ascertain potential anisotropy. From a crystallographic point of view, hexagonal graphite consists of stacks of parallel 2-D graphene sheets with carbon atoms that are arranged in six-fold hexagonal rings through localized in-plane 2s, 2px, and 2py (sp^2) orbitals. The individual sheets are weakly bonded by delocalized out-of-plane 2pz orbitals, which overlap to give a delocalized electron system. Hexagonal graphite crystallizes in the D^4_{6h} point group. The anisotropic graphite structure suggests different properties along different crystallographic axes, namely, very high in-plane strength but very weak out-of-plane strength. Conversely, poorly crystalline graphitic-like carbon or disordered sp^2 carbonaceous materials are composed of polyaromatic clusters that are graphite-like domains typically consisting of 3–4 turbostratically stacked graphene layers (termed *basic structural units* or BSU after Oberlin *et al.,* 1980), with average lateral extensions (microcrystallite planar dimension L_a) of up to 3–100 nm (Bonijoly *et al.,* 1982). These BSU are grafted together by cross-linking

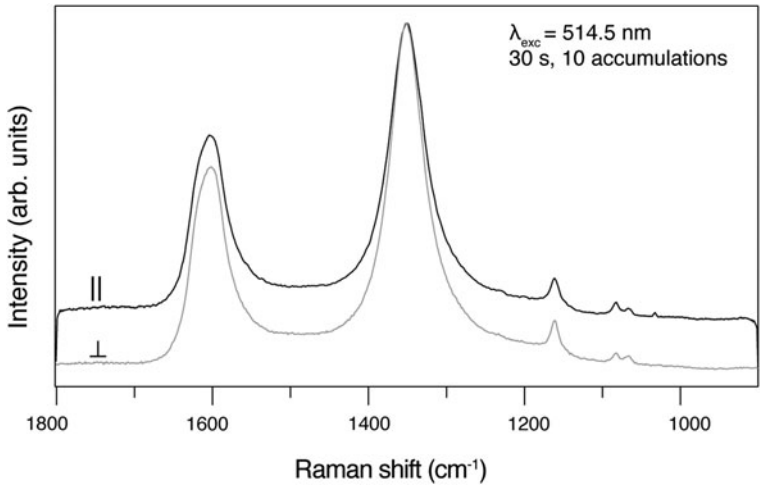

FIG. 3. Plot of Raman spectra acquired from disordered sp^2 carbon from the Apex chert with the incident laser beam either perpendicular or parallel to the *c* axis. The spectrum colored black was acquired with the incident laser beam parallel (||) to the *c* axis, and the spectrum colored gray was acquired with the incident laser beam perpendicular (⊥) to the *c* axis.

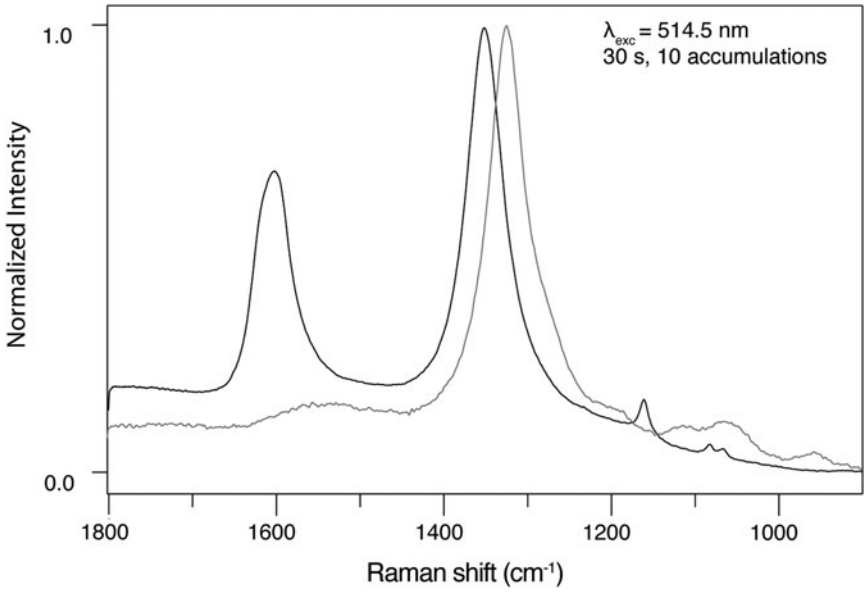

FIG. 4. Plot of Raman spectra collected from research-grade hematite 49-5908 and disordered sp^2 carbonaceous material from a thin section made from the Apex chert showing the coincidence of the hematite 2LO mode (gray spectrum) that is located in the same frequency region of the D band (A_{1g} mode) of disordered sp^2 carbonaceous materials (black spectrum).

heteroatoms (O, S, and N). Therefore, disordered sp^2 carbonaceous material can be considered, crystallographically, hexagonal in symmetry. Hexagonal crystalline solids are anisotropic and can display polarized Raman spectra. Here, we investigate whether the structural anisotropy of disordered sp^2 carbonaceous materials has an effect on Raman spectra with respect to the orientation or direction ($\parallel$ or $\perp$) of the incident laser beam, whether this effect should be considered when generating hyperspectral images from conceivably tens to thousands of spectra from randomly

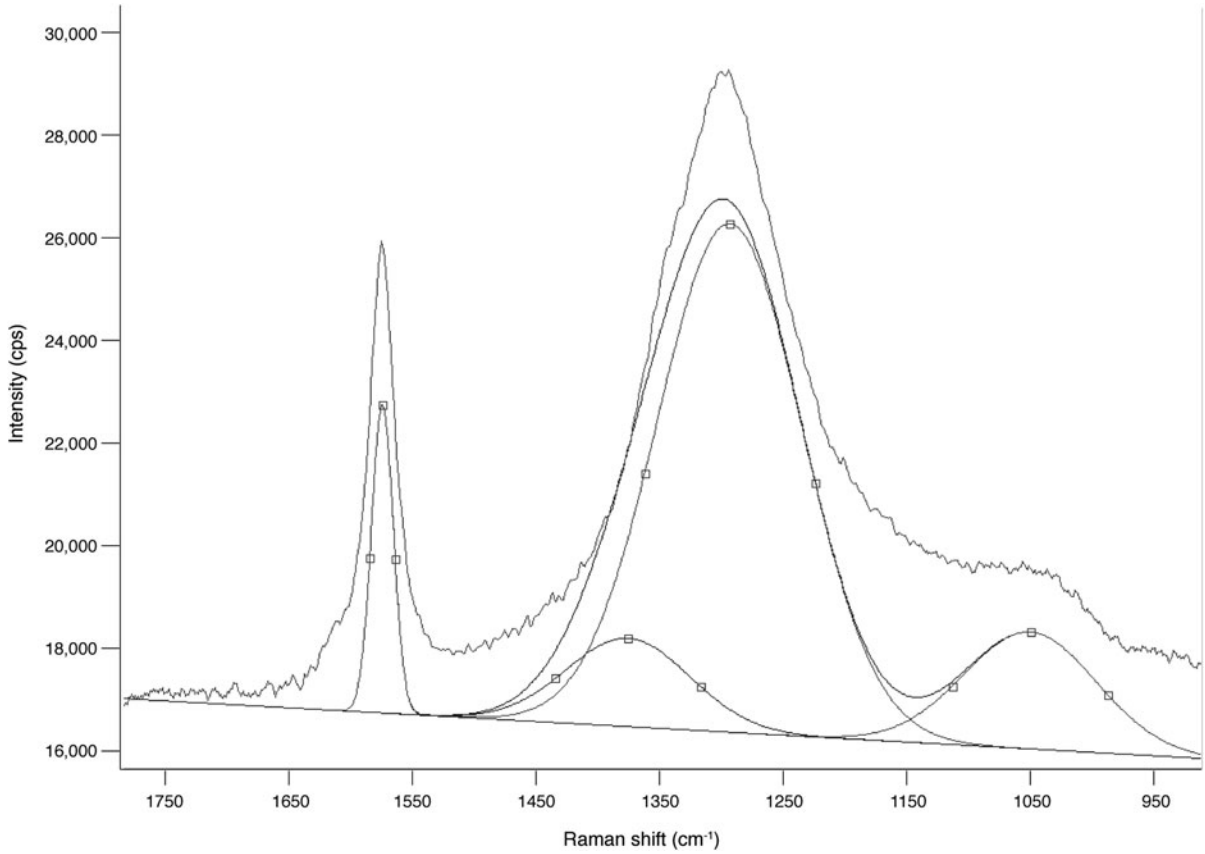

FIG. 5. A Raman spectrum collected on a mixture of research-grade hematite and graphite. This spectrum contains overlapping bands which can be resolved by deconvolution into four Gaussian-Lorentzian components at 1575, 1345, 1300, and 1095 Δ cm^{-1}. The bands at 1575, 1345, and 1300 Δ cm^{-1} are assigned to the G band of sp^2 carbonaceous material, D band of sp^2 carbonaceous material, and the 2LO disordered hematite mode, respectively.

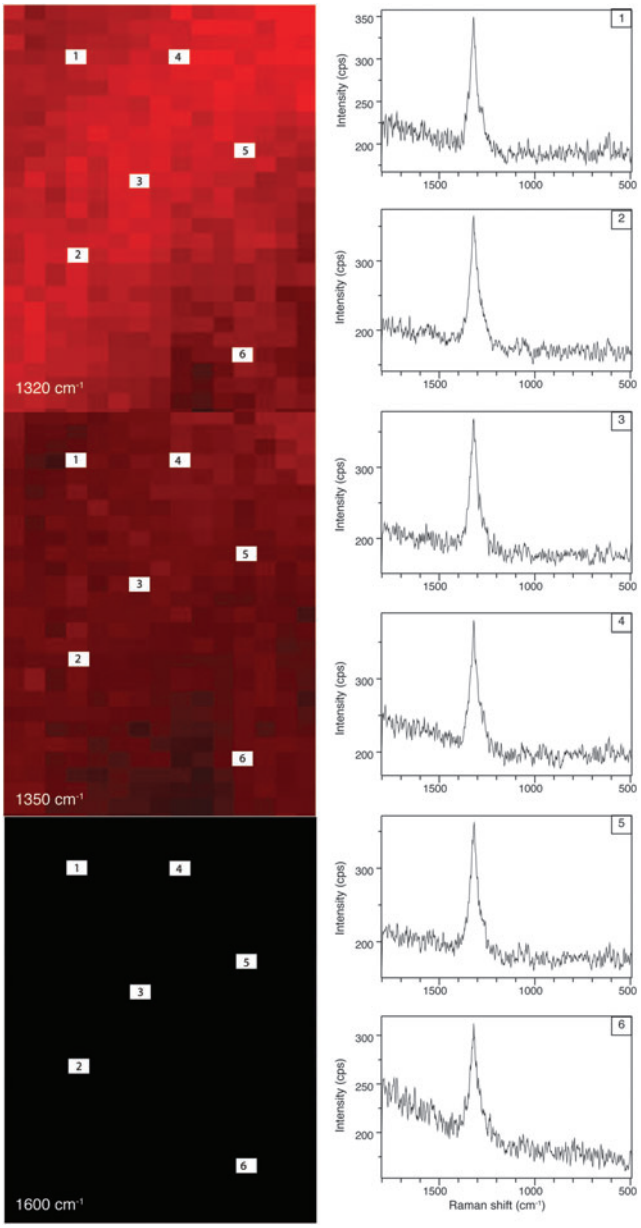

FIG. 6. Hyperspectral images obtained from research-grade hematite 49-5908. Images were generated by using the intensity of the band maxima for the following vibration modes: hematite 2LO mode at 1320 Δ cm^{-1}, D mode (A_{1g}) at 1350 Δ cm^{-1}, and G mode (E_{2g2}) at 1600 Δ cm^{-1}.

orientated crystallites of carbonaceous material in a microstructure of interest, and finally whether this orientation artifact would manifest itself in hyperspectral images.

Our results show that the orientation of crystalline sp^2 carbon with respect to the incident laser beam can have significant effects on the Raman spectrum for highly ordered hexagonal graphite. This observation is in strong agreement with other studies performed on hexagonal graphite and highly orientated pyrolytic graphite (HOPG) (*e.g.,* Katagiri *et al.,* 1988; Wang *et al.,* 1989; Compagnini *et al.,* 1997). If a band has a $\rho < 0.750$ and $\rho > 0.125$, then that band has arisen from a non-degenerate totally symmetric mode. Here, we observe a $\rho = 0.375$, thus the D band has arisen from a non-degenerate totally symmetric mode; therefore the A_{1g} symmetry assignment for the D band is correct. This is in agreement with other experimental symmetry assignment for this mode (*e.g.,* Castiglioni *et al.,* 2005). However, disordered sp^2 carbonaceous materials have a different structure than graphite or HOPG; thus the fact that the Raman spectra of hexagonal graphite and HOPG experience a polarization/orientation effect does not mean that the disordered sp^2 carbonaceous materials will. Our results demonstrate that this effect is insignificant in mid- to low-grade metamorphic disordered sp^2 carbonaceous crystalline materials. This is in a good agreement with the literature (*e.g.,* Jehlička and Bény, 1992; Wopenka and Pasteris, 1993; Aoya *et al.,* 2010; Olcott Marshall *et al.,* 2012a, 2012b).

5.3. Polarization/orientation effects on solid crystalline disordered sp^2 carbonaceous microstructures when generating 2-D and 3-D Raman hyperspectral images

Figure 2 clearly shows that, when dealing with graphite or well-ordered sp^2 carbons from high-grade metamorphic rocks, the intensity of the D band is sensitive to the orientation of the *c* axis with respect to the polarization of the incident light; thus caution should be applied when generating 2-D and 3-D images. From a practical standpoint, it is impossible to maintain a consistent illumination angle of the incident laser (either $\parallel$ or $\perp$) while undertaking 2-D or 3-D imaging of anisotropic crystalline microstructures of interest in thin sections. As a consequence, the resulting hyperspectral 2-D or 3-D image generated from either the D band intensity or D band area or the I_D/I_G ratio would appear to show an erroneous crystallinity or structural order-disorder distributed throughout the image area for that sample. For instance, the point spectra presented by Schiffbauer *et al.* (2007) show D band intensity variation with respect to the angle of the incident laser beam during spectral acquisition. Thus, if 2-D or 3-D images were generated by using the D band intensity or the I_D/I_G ratio from the graphitic discs of Schiffbauer *et al.* (2007), it is likely, given the high-grade metamorphism of these well-ordered sp^2 carbonaceous materials, that images of these microstructures would be affected by this anisotropic artifact. However, our results clearly demonstrate that this anisotropic effect is insignificant for low-grade metamorphic disordered sp^2 carbonaceous materials (Fig. 3). That said, given the possibility of polarization effects, we suggest that the D band intensity should not be used to construct hyperspectral images.

5.4. Spectral misinterpretations

The successful interpretation of Raman spectra is much more than simply assigning group frequencies to a particular band. While interpreting spectra, it should be borne in mind that a successful interpretation is based not only on the presence of a particular band within a spectrum but also the absence of other important bands. The correct identification of a crystalline solid can be rapidly excluded during the interpretation by the use of what vibrational spectroscopists call the *no-band information*. Coincidently, the hematite 2LO mode is located in the frequency region of the D band (A_{1g} mode) from sp^2 carbonaceous materials (Fig. 4). Unfortunately, the broad second-order 2LO 1320 Δ cm^{-1} hematite mode is often mistaken in the materials and geosciences literature for the broad D band (A_{1g} mode) of

disordered sp^2 carbonaceous materials (*e.g.,* Toporski *et al.,* 2004; Lu *et al.,* 2007, 2008). To complicate the issue, it is convention to collect Raman spectra of potential carbonaceous materials with a green laser (either 514.5 or 532 nm) (see Marshall *et al.,* 2010), where the hematite 1320 Δ cm^{-1} 2LO mode becomes strongly enhanced by blue-green excitation. Additionally, in poorly crystalline hematite the 2LO mode at 1320 Δ cm^{-1} can be the most distinctive hematite mode in the whole spectrum (Kremer *et al.,* 2012b). It is noteworthy to point out that several Fe-oxide and Fe-oxyhydroxide minerals also exhibit strong Raman scattering in the 1300–1600 Δ cm^{-1} region. Most of these broad intense bands can be assigned to 2LO modes occurring in the same region as the D band. Table 1 shows band positions for 2LO modes for various Fe-oxide and Fe-oxyhydroxide minerals in the 1300–1600 Δ cm^{-1} region. Thus, the broad intense 2LO band of Fe-oxide and Fe-oxyhydroxide minerals in the 1300–1600 Δ cm^{-1} region can act as a false positive for the identification of carbonaceous material.

The misidentification of the hematite mode as a carbon mode is a prime example of the no-band information. Whether or not the sp^2 carbonaceous network contains structural defects, reduced crystallite size, or graphene planes that are bent, the E_{2g2} mode—the doubly degenerate bond stretching of all pairs of sp^2 carbon atoms, which is often called the G band—will always be present in a Raman spectrum. The G mode is independent of the stacking sequence and does not require the presence of six-fold rings; hence it occurs at all sp^2 sites within the carbon network lattice. Thus, it is impossible that a Raman spectrum of disordered sp^2 carbon will only contain the D band regardless of the degree of structural disorder. Therefore, a spectrum acquired in the carbon first-order region only revealing one broad band at 1320 Δ cm^{-1} should not be assigned to carbon.

Hematite and sp^2 carbonaceous materials can co-occur as mixed opaque phases in sediments, rocks, and meteorites (*e.g.,* Burchell *et al.,* 2006; Mahaney *et al.,* 2010, 2011; Marshall and Olcott Marshall *et al.,* 2011). The Raman spectra obtained on these mixed phases require careful interpretation, as this mixture produces a broad band between 1180 and 1450 Δ cm^{-1} centered at 1300 Δ cm^{-1} with a shoulder at 1345 Δ cm^{-1}, and a narrow band centered at 1575 Δ cm^{-1} (Fig. 5). The line-shape, shoulder, and band positions are indicative of a Raman spectrum collected from a mixed hematite and sp^2 carbonaceous material phase. The bands at 1575, 1345, and 1300 Δ cm^{-1} are assigned to the G band of sp^2 carbonaceous material, D band of sp^2 carbonaceous material, and the 2LO mode of disordered hematite, respectively.

Table 1. Band Positions for 2LO Modes for Various Fe-Oxide and Fe-Oxyhydroxide Minerals in the 1300–1600 Δ cm^{-1} Region

Fe-oxide and Fe-oxyhydroxide mineral	*Formula*	*Crystallography*	*2LO band position (Δ cm^{-1})*
Goethite	α-FeOOH	orthorombic	1304
Akaganeite	β-FeOOH	monoclinic	1410
Lepidocrocite	γ-FeOOH	orthorombic	1300
Maghemite	γ -Fe_2O_3	cubic or trigonal	1430
6-line ferrihydrite	$Fe(O,OH)_6$	trigonal	1291
2-line ferrihydrite	$Fe(O,OH)_6$	trigonal	1340
Hematite	α-Fe_2O_3	trigonal	1320

The intensity ratio between the D and G bands (I_D/I_G) has been well established since the 1970s as a method to elucidate the structural organization (order vs. disorder) and the degree of crystallinity (well vs. poor) of solid crystalline sp^2 carbonaceous materials (*e.g.,* Tuinstra and Koenig, 1970a, 1970b; Mernagh *et al.,* 1984; Knight and White, 1989; Pasteris and Wopenka, 1991; Jehlička and Bény, 1992; Wopenka and Pasteris, 1993; Yui *et al.,* 1996; Jehlička *et al.,* 2003; Marshall *et al.,* 2010; Olcott Marshall *et al.,* 2012a). The relative intensities of the D and G bands vary with thermal stress, and the I_D/I_G ratio can help elucidate information about the metamorphic grade and temperature geological carbonaceous materials have undergone (*e.g.,* Pasteris and Wopenka, 1991; Jehlička and Bény, 1992; Wopenka and Pasteris, 1993; Yui *et al.,* 1996; Beyssac *et al.,* 2002; Jehlička *et al.,* 2003; Marshall *et al.,* 2010; Olcott Marshall *et al.,* 2012a). After deconvolution, we can calculate the I_D/I_G ratio for the spectrum in Fig. 5. The I_D/I_G ratio is calculated from the relative band intensities of the D band at 1345 Δ cm^{-1} and the G band at 1575 Δ cm^{-1}, yielding a value of 0.29, which indicates that the sp^2 carbonaceous material is highly ordered and consistent with having undergone high thermal stress of granulite or eclogite faces grade metamorphism (*e.g.,* Pasteris and Wopenka, 1991; Wopenka and Pasteris, 1993; Jehlička and Bény, 1999). However, if the band at 1300 Δ cm^{-1} is incorrectly interpreted as the D band, a I_D/I_G ratio of 1.65 is obtained, which is indicative of poorly crystalline disordered sp^2 carbonaceous material and consistent with greenschist facies metamorphism (300–350°C) (*e.g.,* Pasteris and Wopenka, 1991; Jehlička and Bény, 1992; Wopenka and Pasteris, 1993; Yui *et al.,* 1996; Marshall *et al.,* 2001; Beyssac *et al.,* 2002; Jehlička *et al.,* 2003; Marshall *et al.,* 2010; Olcott Marshall *et al.,* 2012a).

Additionally, another point to consider when interrogating Fe-oxide and Fe-oxyhydroxide minerals is that the user must be careful, as these minerals can be photochemically transformed by laser powers great than 1 mW. For example, most of the Fe-oxyhydroxides are photochemically converted to hematite, magnetite can be photochemically converted to hematite, and hematite can be photochemically converted to maghemite, which thus makes it impossible to identify the original mineralogy (*e.g.,* de Faria *et al.,* 1997).

5.5. Selection of spectral region for image generation of putative microfossils

To generate 2-D or 3-D images, spectra should be collected in a carefully chosen range of wavelengths covering the selected bands diagnostically characteristic for the successful identification of the feature of interest. Additionally, this selected spectral region should take into account coincidental bands of the component of interest with other material that may likely be present within the sample, for example, co-occurring carbonaceous material and hematite. Therefore, it is not good spectroscopic practice to rely solely on one defining band for identification of composition, but rather the presence of other vibration/lattice modes should be considered.

Paleobiologists typically examine the mineral fingerprint region (200–800 Δ cm^{-1}) and the carbon first-order region (800–1800 Δ cm^{-1}) separately in order to identify these materials (*e.g.,* Schopf *et al.,* 2010). However, these two spectral

regions cannot be considered separately, due to the overlap of hematite and carbonaceous material vibration modes around 1320–1350 Δ cm^{-1}. Some paleobiologists will construct 2-D and 3-D hyperspectral images from spectra collected in the carbon first-order region (1000–1800 Δ cm^{-1}) only and will use the D band intensity for image construction (*e.g.*, Schopf and Kudryavtsev, 2005, 2009; Schopf *et al.*, 2010). Other paleobiologists do not report the spectral region used to generate the hyperspectral image but nonetheless use the intensity of the D band for image construction (*e.g.*, Cavalazzi *et al.*, 2011; Kremer *et al.*, 2012a; Foucher and Westall, 2013). Furthermore, in some instances hyperspectral images have been produced from the intensity of the D band or the intensity between 1225 and 1450 Δ cm^{-1} despite the knowledge of hematite present within the sample (*e.g.*, Schopf *et al.*, 2010; Kremer *et al.*, 2012a). All these practices can lead to the potential incorrect band assignment of the 2LO hematite mode as the D band from carbonaceous materials.

Also, these studies only show a representative point spectrum (with extended exposure times and higher number of accumulations) collected prior to the hyperspectral imaging analyses and do not show representative raw spectra from the large number of spectra collected to generate the image. Thus, it is not possible for readers to assess the data for problems like misidentified vibration modes, anisotropy effects, and autofluorescence baseline effects. Unlike point spectra Raman analyses in which individual spectra are presented, 2-D and 3-D Raman imaging is employed such that the intensity of the major band found in all the hundreds or thousands of spectra is used to automatically generate an image of the microstructure of interest without the need to manually examine all the spectra. Thus, the resulting data comprise an image that does not show the presence of individual Raman bands.

Figure 6 shows hyperspectral images generated from research-grade hematite 49-5908 when using the following band position intensities: 1320 Δ cm^{-1} for the hematite 2LO mode at 1320, 1350 Δ cm^{-1} (D band) to establish the influence of the 2LO hematite mode on the hyperspectral image, and 1600 Δ cm^{-1} (G band) as a test of a marker band for carbonaceous material. In addition, this figure contains some raw spectra used to generate the image, which now the reader can ascertain if (i) the correct band assignment has been made, (ii) the possible effects due to polarization/orientation have occurred, and (iii) the type of spectral processing undertaken prior to image generation was properly selected. The representative raw spectra (1–6) (Fig. 6) show the presence of a broad intense band at 1320 Δ cm^{-1}, which is assigned to the hematite 2LO mode. An image is generated by using the band intensity maxima at 1320 Δ cm^{-1}, which reveals a bright red false-color image indicating this material is composed of hematite. If instead this broad band were interpreted as the D band of carbonaceous material and used to construct an image with the relative intensity band distribution at 1350 Δ cm^{-1}, the result would be a bright red false-color image that would clearly be influenced by the broad hematite band at 1320 Δ cm^{-1} (Fig. 6). Thus, the resulting image would lead to the false identification of a carbonaceous composition for that feature of interest. Clearly, if we construct an image, using the band intensity position of 1600 Δ cm^{-1}, we would obtain a black-colored image indicating the absence of this vibration mode and therefore demonstrating that this sample is not composed of carbonaceous material. Therefore, like Kremer *et al.* (2012b), we suggest that the intensity of the G band position should be selected to generate the hyperspectral image and thus act as a marker band for the successful identification of a carbonaceous composition.

We suggest that it is good practice within the astrobiological and paleobiological communities to use Raman spectroscopy to (i) collect the spectra for the 2-D or 3-D Raman images over the spectral region of 400–1800 Δ cm^{-1}; (ii) avoid any misinterpretation between the uncharacteristically broad 2LO hematite band at 1320 Δ cm^{-1} as the D band (A_{1g}) of disordered sp^2 hybridized carbonaceous materials such that the band of choice to generate the Raman image is the G band (E_{2g2}) at 1600 Δ cm^{-1}; and (iii) include representative examples of raw spectra collected that are used to generate the 2-D or 3-D Raman images, like that shown in Fig. 6. In the case of a sample consisting of a mixed phase of sp^2 carbonaceous material and hematite, we recommend that two images should be generated to distinguish the spatial distribution between the two materials. The first image should be generated from the dominant vibration mode considered diagnostic for hematite, which is the v_sFe-O symmetric stretch with A_{1g} symmetry at *ca.* 225 Δ cm^{-1}. The second image should be generated from the G band (E_{2g2}) at 1600 Δ cm^{-1}.

5.6. Implications for the search for fossilized ancient life

Ancient black chert samples, the most frequent target in the search for ancient life, are challenging to analyze with Raman spectroscopy and often generate complicated spectral responses that should be considered either in the way the data are pre-processed or the interpretation of the resultant images is made. Additionally, these samples are difficult to image with Raman spectroscopy due to their composition. Opaque materials such as black chert and carbonaceous materials have high extinction coefficients for visible light, thus resulting in a low penetration of the laser. Also, these samples undergo autofluorescence due to the presence of thermally immature carbonaceous materials or rare earth elements; they are often heterogeneous, and Raman scattering cross sections vary for different mineralogy, the embedded microstructures vary in topography over a defined imaged area, and polarization effects for anisotropic materials are difficult to take into account. Therefore, caution should be exercised when collecting Raman spectra, interpreting Raman spectra, and processing Raman spectra and hyperspectral images derived from these materials.

Raman microspectroscopy and hyperspectral imaging are becoming increasingly popular in geoscience applications, as geologists, paleontologists, astrobiologists, and planetary and space scientists discover the wealth of nondestructive mineral and mineraloid data that Raman microspectroscopy can provide. As Raman microspectroscopy is rapidly becoming a technique used by non-Raman spectroscopists, Raman spectrometers are becoming increasingly automated, and the interpretation of data is becoming increasingly database-driven. Thus, while some are cognizant of the overlap between the second-order 2LO *ca.* 1320 Δ cm^{-1} mode of

hematite and the *ca.* 1350 Δ cm^{-1} disordered sp^2 hybridized carbonaceous material D band (A_{1g} mode) (*e.g.,* Zajickova *et al.,* 2009; Mahaney *et al.,* 2010, 2011; Marshall *et al.,* 2011; Marshall and Olcott Marshall, 2011; Edwards *et al.,* 2013), many remain unaware and identify hematite by examination of the mineral fingerprint region only (200–800 Δ cm^{-1}) and carbonaceous material by examination of the carbon first-order region only (*e.g.,* Schopf *et al.,* 2010). The best way to present Raman data of samples that contain both optically opaque hematite and sp^2 carbonaceous material is to show spectra collected in the 100–1800 Δ cm^{-1} region to allow the identification of carbonaceous material and hematite vibration modes and hence avoid spectral misinterpretations. In addition, some of the most popular online Raman spectroscopic databases do not mention the hematite band at *ca.* 1320 Δ cm^{-1} (Downs, 2006; Laboratoire de Sciences de la Terre, 2010). Furthermore, Raman spectrometer vendors have even misidentified hematite as disordered sp^2 hybridized carbonaceous material (*e.g.,* www.witec.de/en/download/Raman/geoscience.pdf—Fig. 5). In this case, the opaque material that was analyzed was poorly crystalline hematite where the most intense vibration mode was the 2LO mode at 1320 Δ cm^{-1} and the normally most intense bands typically used to identify hematite, that is, the E_g modes at 292 and 411 Δ cm^{-1}, were very weak. As a consequence, it is easy for a non-Raman spectroscopist to misidentify hematite as disordered sp^2 hybridized carbonaceous material.

6. Conclusion

Over the last decade, Raman microspectroscopy and hyperspectral imaging have become very powerful techniques with applications in astrobiology and paleobiology to elucidate a carbonaceous composition for putative microfossils. Raman spectroscopic data must be modeled carefully in order to extract meaningful quantitative results; otherwise band assignments and the depth scale and size of buried microstructures are grossly incorrect and can lead to erroneous interpretations about the fossil evidence of early life on Earth. Care must be taken to distinguish between the broad hematite disorder mode at *ca.* 1320 Δ cm^{-1} and that of the disordered sp^2 hybridized carbonaceous D mode at *ca.* 1350 Δ cm^{-1}. To avoid misinterpreting the disorder mode of hematite with the disorder mode of sp^2 carbonaceous material, and to take into account anisotropic effects, we strongly recommend that the hundreds to thousands of spectra used to generate 2-D and 3-D Raman images should first be collected over the spectral region of 400–1800 Δ cm^{-1}. The only choice of Raman band to use for image construction should be the G mode at *ca.* 1600 Δ cm^{-1}. In the end, each image figure should show representative raw spectra used in generating the image.

Acknowledgments

This work is supported by NSF grant EAR-1053241. We thank the efforts of two anonymous reviewers for improving our manuscript.

Disclosure Statement for All the Authors

No competing financial interests exist.

Abbreviations

BSU, basic structural units; HOPG, highly orientated pyrolytic graphite; LO, longitudinal optical; NA, numerical aperture; NIR, near-IR; RI, refractive index; TO, traversal optical; vis, visible.

References

Aoya, M., Kouketsu, Y., Endo, S., Shimizu, H., Mizukami, T., Nakamura, D., and Wallis, S. (2010) Extending the applicability of the Raman carbonaceous-material geothermometer using data from contact metamorphic rocks. *Journal of Metamorphic Geology* 28:895–914.

Beyssac, O., Goffe, B., Chopin, C., and Rouzaud, J.-N. (2002) Raman spectra of carbonaceous material in metasediments: a new geothermometer. *Journal of Metamorphic Geology* 20: 859–871.

Bonijoly, M., Oberlin, M., and Oberlin, A. (1982) A possible mechanism for natural graphite formation. *International Journal of Coal Geology* 1:283–312.

Burchell, M.J., Mann, J., Creighton, J.A., Kearsley, A.T., Graham, G., and Franchi, I.A. (2006) Identification of minerals and meteoritic materials via Raman techniques after capture in hypervelocity impacts on aerogel. *Meteorit Planet Sci* 41: 217–232.

Castiglioni, C., Tommasin, M., Zamboni, M., Brambilla, L., Zerbi, G., and Mullen, K. (2005) Experimental symmetry assignment of the D band: evidence from the Raman spectra of soluble "molecular graphite." *AIP Conf Proc* 786:174–177.

Cavalazzi, B., Westall, F., Cady, S.L., Barbieri, R., and Foucher, F. (2011) Potential fossil endoliths in vesicular pillow basalt, Coral Patch Seamount, eastern North Atlantic Ocean. *Astrobiology* 11:619–632.

Compagnini, G., Puglist, O., and Foti, G. (1997) Raman spectra of virgin and damaged graphite edge planes. *Carbon* 35:1793–1797.

de Faria, D.L.A., Venancio Silva, S., and de Oliveria, M.T. (1997) Raman microspectroscopy of some iron oxides and oxyhydroxides. *J Raman Spectrosc* 28:873–878.

Delhaye, M. and Dhamelincourt, P. (1975) Raman microprobe and microscope with laser excitation. *J Raman Spectrosc* 3:33–43.

Des Marais, D.J., Nuth, J.A., Allamandola, L.J., Boss, A.P., Farmer, J.D., Hoehler, T.M., Jakosky, B.M., Meadows, V.S., Pohorille, A., Runnegar, B., and Spormann, A.M. (2008) The NASA Astrobiology Roadmap. *Astrobiology* 8:715–730.

Downs, R.T. (2006) The RRUFF Project: an integrated study of the chemistry, crystallography, Raman and infrared spectroscopy of minerals. In *19th General Meeting of the International Mineralogical Association,* Kobe, Japan, pp 3–13.

Edwards, H.G.M., Jorge Villar, S.E., Pullan, D., Hofmann, B.A., Hargreaves M.D., and Westall, F. (2007) Morphological biosignatures from relict fossilised sedimentary geological specimens: a Raman spectroscopic study. *J Raman Spectrosc* 38:1352–1361.

Edwards, H.G.M., Hutchinson, I.B., Ingley, R., Parnell, J., Vitek, P., and Jehlička, J. (2013) Raman spectroscopic analysis of geological and biological specimens of relevance to the ExoMars mission. *Astrobiology* 13:543–549.

Everall, N.J. (2000) Modeling and measuring the effect of refraction on the depth resolution of confocal Raman microspectroscopy. *Appl Spectrosc* 54:773–782.

Foucher, F. and Westall, F. (2013) Raman imaging of metastable opal in carbonaceous microfossils of the 700–800 Ma old Draken Formation. *Astrobiology* 13:57–67.

Jehlička, J. and Bény, C. (1992) Application of Raman microspectroscopy in the study of structural changes in Precambrian kerogens during regional metamorphism. *Org Geochem* 18:211–213.

Jehlička, J. and Bény, C. (1999) First and second order Raman spectra of natural highly carbonified organic compounds from metamorphic rocks. *J Mol Struct* 480–481:541–545.

Jehlička, J., Urban, O., and Pokorný, J. (2003) Raman spectroscopy of carbon and solid bitumens in sedimentary and metamorphic rocks. *Spectrochim Acta A Mol Biomol Spectrosc* 59:2341–2352.

Katagiri, G., Ishida, H., and Ishitani, A. (1988) Raman spectra of graphite edge plane. *Carbon* 26:565–571.

Kazmierczak, J. and Kremer, B. (2009) Spore-like bodies in early Paleozoic acritarchs: clues to chlorococcalean affinities. *Acta Palaeontol Pol* 54:541–551.

Knight, D.S. and White, W.B. (1989) Characterization of diamond films by Raman spectroscopy. *J Mater Res* 4:385–393.

Kremer, B., Bauer, M., Stark, R.W., Gast, N., Altermann, W., Gursky, H.-J., Heckl, W.M., and Kazmierczak, J. (2012a) Laser-Raman and atomic force microscopy assessment of the chlorococcalean affinity of problematic microfossils. *J Raman Spectrosc* 43:32–39.

Kremer, B., Owocki, K., Krolikowska, A., Wrzosek, B., and Kazmierczak, J. (2012b) Mineral microbial structures in a bone of the Late Cretaceous dinosaur *Saurolophus angustirostris* from the Gobi Desert, Mongolia—a Raman spectroscopy study. *Palaeogeogr Palaeoclimatol Palaeoecol* 358–360:51–61.

Laboratoire de Sciences de la Terre (2010) *Handbook of Minerals Raman Spectra*. http://www.ens-lyon.fr/LST/Raman/ (accessed September 2013).

Lespade, P., Marchand, A., Couzi, M., and Cruege, F. (1984) Caracterisation de materiaux carbones par microspectrometrie Raman. *Carbon* 22:375–385.

Lu, Z., Cheng, H., Lo, M., and Chung, C.Y. (2007) Pulsed laser deposition and electrochemical characterization of $LiFePO_4$–Ag composite thin films. *Adv Funct Mater* 17:3885–3896.

Lu, Z.G., Lo, M.F., and Chung, C.Y. (2008) Pulse laser deposition and electrochemical characterization of $LiFePO_4$–C composite thin films. *J Phys Chem C Nanomater Interfaces* 112: 7069–7078.

Mahaney, W.C., Kalm, V., Krinsley, D.H., Tricart, P., Schwartz, S., Dohm, J., Kim, K.L., Kapran, B., Milner, M.W., Beukens, R., Boccia, S., Hancock, R.G.V., Hart, K.M., and Kelleher, B. (2010) Evidence from the northwestern Venezuelan Andes for extraterrestrial impact: the black mat enigma. *Geomorphology* 116:48–57.

Mahaney, W.C., Krinsley, D.H., Langworthy, K., Kalm, V., Havics, T., Hart, K.M., Kelleher, B.P., Schwartz, S., Tricart, P., and Beukens, R. (2011) Fired glaciofluvial sediment in the northwestern Andes: biotic aspects of the black mat. *Sedimentary Geology* 237:73–83.

Marshall, C.P. and Olcott Marshall, A. (2011) Hematite and carbonaceous materials in geological samples: a cautionary tale. *Spectrochim Acta A Mol Biomol Spectrosc* 80:133–137.

Marshall, C.P., Mar, G.L., Nicoll, R.S., and Wilson, M.A. (2001) Organic geochemistry of artificially matured conodonts. *Org Geochem* 32:1055–1071.

Marshall, C.P., Edwards, H.G.M., and Jehlička, J. (2010) Understanding the application of Raman spectroscopy to the detection of traces of life. *Astrobiology* 10:229–243.

Marshall, C.P., Emry, J.R., and Olcott Marshall, A. (2011) Haematite pseudomicrofossils present in the 3.5-billion-year-old Apex chert. *Nat Geosci* 4:240–243.

McCreery, R.L. (2000) *Raman Spectroscopy for Chemical Analysis,* Wiley-Interscience, New York.

Mernagh, T.P., Cooney, R.P., and Johnson, R.A. (1984) Raman spectra of graphon carbon black. *Carbon* 22:39–42.

Meyer, M., Schiffbauer, J.D., Xiao, S., Cai, J., and Hua, H. (2012) Taphonomy of the Upper Ediacaran enigmatic ribbonlike fossil Shaanxilithes. *Palaios* 27:354–372.

Oberlin, A., Boulmier, J.L., and Villey, M. (1980) Electron microscopic study of kerogen microtexture. Selected criteria for determing the evolution path and evolution stage of kerogen. In *Kerogen,* edited by B. Durand, Technip, Paris, pp 191–241.

Olcott Marshall, A., Emry, J.E., and Marshall, C.P. (2012a) Multiple generations of carbon in the Apex chert and implications for preservation of microfossils. *Astrobiology* 12:160–166.

Olcott Marshall, A., Wehrbein, R.L., Lieberman, B.S., and Marshall, C.P. (2012b) Raman spectroscopic investigations of Burgess Shale–type preservation: a new way forward. *Palaios* 27:288–292.

Pasteris, J.D. and Wopenka, B. (1991) Raman spectra of graphite as indicators of degree of metamorphism. *Can Mineral* 29: 143–153.

Pflug, H.D. (1984) *Die Spur des Lebens,* Springer, Berlin.

Pflug, H.D. and Jaeschke-Boyer, H. (1979) Combined structural and chemical analysis of 3,800-Myr-old microfossils. *Nature* 280:483–486.

Raman, C.V. (1928) A new radiation. *Indian Journal of Physics* 2:387–398.

Raman, C.V. and Krishnan, K.S. (1928a) A new type of secondary radiation. *Nature* 121:501.

Raman, C.V. and Krishnan, K.S. (1928b) A new class of spectra due to secondary radiation part 1. *Indian Journal of Physics* 2:399–419.

Rosasco, G.J., Etz, E.S., and Cassatt, W.A. (1975) The analysis of discrete fine particles by Raman spectroscopy. *Appl Spectrosc* 29:396–404.

Schiffbauer, J.D., Yin, L., Bodnar, R., Kaufman, A.J., Meng, F., Hu, J., Shen, B., Yuan, X., Bao, H., and Xiao, S. (2007) Ultrastructural and geochemical characterization of Archean Paleoproterozoic graphite particles: implications for recognizing traces of life in highly metamorphosed rocks. *Astrobiology* 7:684–704.

Schiffbauer, J.D., Wallace, A.F., Hunter, J.I., Jr., Kowalewski, M., Bodnar, R.J., and Xiao, S. (2012) Thermally-induced structural and chemical alteration of organic-walled microfossils: an experimental approach to understanding fossil preservation in metasediments. *Geobiology* 10:402–423.

Schopf, J.W. and Kudryavtsev, A.B. (2005) Three-dimensional Raman imagery of Precambrian microscopic organisms. *Geobiology* 3:1–12.

Schopf, J.W. and Kudryavtsev, A.B. (2009) Confocal laser scanning microscopy and Raman imagery of ancient microscopic fossils. *Precambrian Res* 173:39–49.

Schopf, J.W. and Kudryavtsev, A.B. (2012) Biogenicity of Earth's earliest fossils: a resolution of the controversy. *Gondwana Research* 22:761–771.

Schopf, J.W., Kudryavtsev, A.B., Agresti, D.G., Wdowiak, T.J., and Czaja, A.D. (2002) Laser-Raman imagery of Earth's earliest fossils. *Nature* 416:73–76.

Schopf, J.W., Kudryavtsev, A.B., Sugitani, K., and Walter, M.W. (2010) Precambrian microbe-like pseudofossils: a promising solution to the problem. *Precambrian Res* 179:191–205.

Toporski, J., Fries, M., Steele, A., Nittler, L., and Kress, M. (2004) Sweeping the skies: stardust and the origin of our Solar System. *Imaging and Microscopy* 4:38–40.

Tuinstra, F. and Koenig, J.L. (1970a) Raman spectrum of graphite. *J Chem Phys* 53:1126–1130.

Tuinstra, F. and Koenig, J.L. (1970b) Characterization of graphite fiber surfaces with Raman spectroscopy. *J Compos Mater* 4: 492–499.

Turrell, G. (1972) *Infrared and Raman Spectra of Crystals,* Academic Press, London.

Ueno, Y., Isozaki, Y., Yurimoto, H., and Maruyama, S. (2001a) Carbon isotopic signatures of individual Archaean microfossils (?) from Western Australia. *Int Geol Rev* 43:196–212.

Ueno, Y., Isozaki, Y., Yurimoto, H., and Maruyama, S. (2001b) Early Archean (*ca.* 3.5) microfossils and ^{13}C-depleted carbonaceous matter in the North Pole area, Western Australia. Field occurrence and geochemistry. In *Geochemistry and the Origin of Life*, edited by S. Nakashima, S. Maruyama, A. Brack, and B.F. Windley, Universal Academy Press, Tokyo, pp 203–236.

Vago, J., Gardini, B., Kminek, G., Baglioni, P., Gianfiglio, G., Santovincenzo, A., Bayon, S., and van Winnendael, M. (2006) ExoMars—searching for life on the Red Planet. *ESA Bull* 126:16–23.

Wang, A., Dhamenincourt, P., Dubessy, J., Guerard, D., Landais, P., and Lelaurain, M. (1989) Characterization of graphite alteration in an uranium deposit by micro-Raman spectroscopy, X-ray diffraction, transmission electron microscopy and scanning electron microscopy. *Carbon* 27:209–218.

Wang, A., Kuebler, K.E., Jolliff, B.L., and Haskin, L.A. (2004) Mineralogy of a martian meteorite as determined by Raman spectroscopy. *J Raman Spectrosc* 35:504–514.

Wang, A., Freeman, J.F., Jolliff, B.L., and Chou, I.M. (2006) Sulfates on Mars: a systematic Raman spectroscopic study of hydration states of magnesium sulfates. *Geochim Cosmochim Acta* 70:6118–6135.

Wopenka, B. (2012) Raman spectroscopic investigation of two grains from comet 81P/Wild 2: information that can be obtained beyond the presence of sp^2-bonded carbon. *Meteorit Planet Sci* 47:565–584.

Wopenka, B. and Pasteris, J.D. (1993) Structural characterization of kerogens to granulite-facies graphite: applicability of Raman microprobe spectroscopy. *Am Mineral* 78: 533–557.

Yui, T.-F., Huang, E., and Xu, J. (1996) Raman spectrum of carbonaceous material: a possible metamorphic grade indicator for low-grade metamorphic rocks. *Journal of Metamorphic Geology* 14:115–124.

Zajickova, L., Syneka, P., Jaseka, O., Eliasa, M., Bohumil, D., Bursik, J., Pizurova, N., Hanzlikova, R., and Lazara, L. (2009) Synthesis of carbon nanotubes and iron oxide nanoparticles in MW plasma torch with Fe(CO) in gas feed. *Appl Surf Sci* 255:5421–5424.

Address correspondence to:
Craig P. Marshall
Department of Geology
University of Kansas
1475 Jayhawk Blvd.
Lawrence KS 66045

E-mail: cpmarshall@ku.edu

Submitted 17 May 2013
Accepted 23 August 2013